

1 Source-Resolved Volatility and Oxidation State Decoupling in 2 Wintertime Organic Aerosols in Seoul

3
4 Hwajin Kim^{1,2,*}, Jiwoo Jeong¹, Jihye Moon¹, Hyun Gu Kang^{2,3}

5 ¹Department of Environmental Health Sciences, Graduate School of Public Health, Seoul National University, 08826 Seoul,
6 South Korea

7 ²Institute of Health and Environment, Graduate School of Public Health, Seoul National University, 08826 Seoul, South Korea

8 ³Now at Multiphase Chemistry Department, Max Planck Institute for Chemistry, 55128 Mainz, Germany

9 Correspondence to: Hwajin Kim (khj0116@snu.ac.kr)

10 Abstract.

11 Organic aerosols (OA) are key components of wintertime urban haze, but the relationship between their oxidation
12 state and volatility—critical for understanding aerosol evolution and improving model predictions—remains poorly
13 constrained. While oxidation–volatility decoupling has been observed in laboratory studies, field-based evidence
14 under real-world conditions is scarce, particularly during severe haze episodes. This study presents a field-based
15 investigation of OA sources and their volatility characteristics in Seoul during a winter haze period, using a
16 thermodenuder coupled with a high-resolution time-of-flight aerosol mass spectrometer (HR-ToF-AMS).

17 Positive matrix factorization resolved six OA factors: hydrocarbon-like OA, cooking, biomass burning, nitrogen-
18 containing OA (NOA), less-oxidized oxygenated OA (LO-OOA), and more-oxidized OOA (MO-OOA). Despite
19 having the highest oxygen-to-carbon ratio (~1.15), MO-OOA exhibited unexpectedly high volatility, indicating a
20 decoupling between oxidation state and volatility. We attribute this to fragmentation-driven aging and autoxidation
21 under stagnant conditions with limited OH exposure. In contrast, LO-OOA showed lower volatility and more
22 typical oxidative behavior.

23 Additionally, NOA—a rarely resolved factor in wintertime field studies—was prominent during cold, humid, and
24 stagnant conditions and exhibited chemical and volatility features similar to biomass burning OA, suggesting a
25 shared combustion origin and meteorological sensitivity.

26 These findings provide one of the few field-based demonstrations of oxidation–volatility decoupling in ambient
27 OA and highlight how source-specific properties and meteorology influence OA evolution. The results underscore
28 the need to refine OA representation in chemical transport models, especially under haze conditions.

29

30 **Keywords:** Organic aerosol volatility, HR-ToF-AMS, Thermodenuder, elemental ratios, aging, fragmentation

31 **1 Introduction**

32 Atmospheric aerosols affect both human health and the environment by reducing visibility (Ghim et al., 2005; Zhao
33 et al., 2013) and contributing to cardiovascular and respiratory diseases (Hamanaka et al., 2018; Manisalidis et al.,
34 2020). In addition, aerosols play a significant role in climate change by scattering or absorbing solar radiation and
35 modifying cloud properties (IPCC AR6). Among the various aerosol components—including sulfate, nitrate,
36 ammonium, chloride, crustal materials, and water—organic aerosols (OA) are particularly important to characterize,
37 as they account for 20–90% of submicron particulate matter (Zhang et al., 2007). Identifying OA sources and
38 understanding their behavior are critical for effective air quality management; however, this is particularly
39 challenging due to the vast diversity and dynamic nature of OA compounds, which originate from both natural and
40 anthropogenic sources. Unlike inorganic aerosols, organic aerosols (OAs) evolve continuously through complex
41 atmospheric reactions, influenced by emission sources, meteorological conditions, and aerosol properties (Jimenez
42 et al., 2009; Hallquist et al., 2009; Robinson et al., 2007; Donahue et al., 2006; Ng et al., 2010; Cappa and Jimenez,
43 2010).

44 Volatility is a key parameter for characterizing organic aerosol (OA) properties, as it governs gas-to-particle
45 partitioning behavior and directly influences particle formation yields (Sinha et al., 2023). The classification of OA
46 species based on their volatility—from extremely low-volatility (ELVOC) to semi-volatile (SVOC) and intermediate-volatility
47 (IVOC) compounds—is central to the conceptual framework of secondary OA (SOA) formation and growth (Donahue et al.,
48 2006). It also affects atmospheric lifetimes and human exposure by determining how long aerosols remain
49 suspended in the atmosphere (Glasius and Goldstein, 2016). Therefore, accurately capturing OA volatility is
50 essential for improving predictions of OA concentrations and their environmental and health impacts. However,
51 chemical transport models often significantly underestimate OA mass compared to observations (Matsui et al.,
52 2009; Jiang et al., 2012; Li et al., 2017), largely due to incomplete precursor inventories and simplified treatment
53 of processes affecting OA volatility. For instance, aging—through oxidation reactions such as functionalization
54 and fragmentation—can significantly alter volatility by changing OA chemical structure (Robinson et al., 2007;
55 Zhao et al., 2016). Early volatility studies primarily utilized thermal denuders (TD) coupled with various detection
56 instruments to investigate the thermal properties of bulk OA (Huffman et al., 2008). The subsequent coupling of TD with the
57 Aerosol Mass Spectrometer allowed for component-resolved volatility measurements, providing critical, quantitative insight
58 into the properties of OA factors (e.g., SV-OOA vs. LV-OOA) across different regions (Paciga et al., 2016; Cappa and Jimenez,
59 2010). These component-resolved volatility data are often used to constrain the Volatility Basis Set (VBS)—the current state-
60 of-the-art framework for modeling OA partitioning and evolution (Donahue et al., 2006). However, a limitation in many field
61 studies is that the TD-AMS thermogram data are rarely translated into quantitative VBS distributions for individual OA factors,

Formatted: Font color: Auto

Formatted: Font: Not Bold, Font color: Auto

Formatted: Font color: Auto

Formatted: Font: Not Bold, Font color: Auto

Formatted: Font color: Auto

62 which limits their direct use in chemical transport models. Furthermore, the volatility of OOA during extreme haze conditions,
63 where the expected inverse correlation between oxidation (O:C) and volatility can break down (Jimenez et al., 2009), remains
64 poorly characterized, particularly in East Asia's highly polluted winter environments. A recent study in Korea further
65 highlighted the importance of accounting for such processes when interpreting OA volatility under ambient
66 conditions (Kang et al., 2023). Given its central role in OA formation, reaction, and atmospheric persistence,
67 volatility analysis is critical for bridging the gap between measurements and model performance.

68 Traditionally, due to the complexity and variability of OA, the oxygen-to-carbon (O:C) ratio has been used as a
69 proxy for estimating volatility. In general, higher O:C values indicate greater oxidation and lower volatility
70 (Jimenez et al., 2009). Accordingly, many field studies classify oxygenated OA (OOA) into semi-volatile OOA
71 (SV-OOA) and low-volatility OOA (LV-OOA) based on their O:C ratios (Ng et al., 2010; Huang et al., 2010; Mohr
72 et al., 2012). However, this relationship is not always straightforward. Fragmentation during oxidation can increase
73 both O:C and volatility simultaneously, disrupting the expected inverse correlation (Jimenez et al., 2009). In
74 laboratory experiments, yields of highly oxidized SOA have been observed to decrease due to fragmentation (Xu
75 et al., 2014; Grieshop et al., 2009). These findings suggest that while O:C can offer useful insights, it is insufficient
76 alone to represent OA volatility. Direct volatility measurements, especially when paired with chemical composition
77 data, are necessary to improve our understanding of OA sources and aging processes.

78 In this study, we investigate the sources and volatility characteristics of OA in Seoul during winter. Wintertime OA
79 presents additional challenges due to its high complexity. During winter, emissions from combustion sources such
80 as biomass burning and residential heating significantly increase, contributing large amounts of primary OA (Kim
81 et al., 2017). Meanwhile, low ambient temperatures and reduced photochemical activity affect the formation and
82 evolution of secondary OA (SOA). Frequent haze events further complicate the aerosol properties by extending
83 aging times and increasing particle loadings. These overlapping sources and atmospheric conditions make winter
84 OA particularly difficult to characterize and predict. ~~Seoul, however, comprehensive studies on OA volatility~~
85 ~~during winter remain limited, despite the season's significance for air quality management. Despite Seoul's~~
86 ~~significance for air quality management, comprehensive studies on OA volatility during winter remain limited.~~ To address
87 these goals, we conducted real-time, high-resolution measurements using a high-resolution time-of-flight aerosol
88 mass spectrometer (HR-ToF-AMS) coupled with a thermodenuder (TD). The objectives of this study are to: (1)

Formatted: Font color: Auto

Formatted: Font color: Auto

89 improve the understanding of wintertime OA in Seoul, (2) characterize the volatility of OA associated with different
90 sources, and (3) explore the relationship between OA volatility and chemical composition.

Formatted: Font color: Auto

91 2 Experimental methods

92 2.1 Sampling Site and Measurement Period

93 We conducted continuous real-time measurements in Seoul, South Korea, from 28 November to 28 December
94 2019. The sampling site was located in the northeastern part of the city (37.60° N, 127.05° E), approximately 7 km
95 from the city center, surrounded by major roadways and mixed commercial–residential land use. Air samples were
96 collected at an elevation of approximately 60 meters above sea level, on the fifth floor of a building. A detailed site
97 description has been reported previously for winter Seoul (Kim et al., 2017). During this period, the average
98 ambient temperature was 1.76 ± 4.3 °C, and the average relative humidity (RH) was $56.9 \pm 17.5\%$, based on data
99 from the Korea Meteorological Administration (<http://www.kma.go.kr>).

Formatted: Font: Not Bold, Font color: Auto

100 Continuous real time measurements were conducted in Seoul, the capital of South Korea, where a previous study
101 (Kim et al., 2017) was also performed. Detailed descriptions of the measurement site can be found in that reference.
102 Briefly, the sampling site was located in the northeastern part of the city (37.60° N, 127.05° E), approximately 7
103 km from the city center. Air samples were collected at an elevation of approximately 60 meters above sea level, on
104 the fifth floor of a building. The site is situated near major expressways and is surrounded primarily by commercial
105 and residential areas, indicating substantial influence from anthropogenic and primary emission sources (Kim et
106 al., 2017). Measurements were carried out from November 28 to December 28, 2019. During this period, the
107 average ambient temperature was 1.76 ± 4.3 °C, and the average relative humidity (RH) was $56.9 \pm 17.5\%$, based
108 on data from the Korea Meteorological Administration (<http://www.kma.go.kr>).

Formatted: Font color: Auto

Formatted: Font: Not Bold, Font color: Auto

Formatted: Font: Not Bold

Formatted: Font: Not Bold, Font color: Auto

Formatted: Font color: Auto

109 2.2 Instrumentation and Measurements

110 The physico-chemical properties of non-refractory PM₁ (NR-PM₁) species—including sulfate, nitrate, ammonium,
111 chloride, and organics—were measured using an Aerodyne high-resolution time-of-flight aerosol mass
112 spectrometer (HR-ToF-AMS) (DeCarlo et al., 2006). PM₁ mass in this study is taken as NR-PM₁ (from AMS) +
113 black carbon (BC; measured by MAAP), which is appropriate for winter Seoul where refractory PM₁ (metal/sea-
114 salt/crustal) is minor and dust events were excluded (e.g., Kim et al., 2017; Nault et al., 2018; Kang et al., 2022;
115 Jeon et al., 2023). Data were acquired at 2.5-minute intervals, alternating between V and W modes. The V mode

Field Code Changed

Formatted: Font color: Auto

Formatted: Font color: Auto

Formatted: Font color: Auto

116 provides higher sensitivity but lower resolution, suitable for mass quantification, whereas the W mode offers higher
117 mass resolution but lower sensitivity, used here for OA source apportionment. Simultaneously, black carbon (BC)
118 concentrations were measured at 1-minute intervals using a multi-angle absorption photometer (MAAP; Thermo
119 Fisher Scientific, Waltham, MA, USA). Total PM₁ mass was calculated as the sum of NR-PM₁ and BC.

120 Hourly trace gas concentrations (CO, O₃, NO₂, SO₂) were obtained from the Gireum air quality monitoring station
121 (37.61° N, 127.03° E), managed by the Seoul Research Institute of Public Health and Environment. Meteorological
122 data (temperature, RH, wind speed/direction) were collected from the nearby Jungreung site (37.61° N, 127.00°
123 E). All data are reported in Korea Standard Time (UTC+9).

124 To examine aerosol volatility, a thermodenuder (TD; Envalytix LLC) was installed upstream of the HR-ToF-AMS.
125 Details are provided in Supplementary Section S1 Kang et al. (2022). Briefly, ambient flow alternated every 5
126 minutes between a TD line and a bypass line at 1.1 L min⁻¹. Residence time in the TD line was ~6.3 s. The TD
127 setup included a 50 cm heating section followed by an adsorption unit. Heated particles were stripped of volatile
128 species, while the downstream carbon-packed section prevented recondensation. TD temperature cycled through
129 12 steps (30 to 200 °C), with each step lasting 10 min (total cycle = 120 min). AMS V and W modes were alternated
130 during the same cycle. The heater was pre-adjusted to the next temperature while the bypass was active.

131

132 **2.3 Data Analysis**

133

134 **2.3.1 Data analysis and OA Source Apportionment**

135 HR-AMS data were processed using SQUIRREL v1.65B and PIKA v1.25B. Mass concentrations of non-refractory
136 PM₁ (NR-PM₁) species were derived from V-mode data, while high-resolution mass spectra (HRMS) and the
137 elemental composition of organic aerosols (OA) were obtained from W-mode data. NR-PM₁ quantification
138 followed established AMS protocols (Ulbrich et al., 2009; Zhang et al., 2011). Both the bypass and TD streams
139 were processed using a time-resolved, composition-dependent collection efficiency CE(t) following Middlebrook
140 et al. (2012). TD heating can modify particle water and phase state/mixing and thereby influence CE beyond
141 composition (Huffman et al., 2009), but prior TD-AMS studies indicate that such effects are modest and largely
142 multiplicative, which do not distort thermogram shapes or T₅₀ ordering (Faulhaber et al., 2009; Cappa & Jimenez,
143 2010). In our data, the CE(t) statistics for the two lines were similar (campaign-average CE: TD = 0.55 ± 0.08;
144 bypass = 0.53 ± 0.04; Δ = 0.02 ≈ 3.7%, below the combined uncertainty ≈ 0.09). We therefore report volatility

145 metrics with these line-specific CE(t) corrections applied and interpret potential residual CE effects as minor. For
146 organics. Elemental ratios (O:C, H:C, and OM/OC) were calculated using the Improved-Ambient (IA) method
147 (Canagaratna et al., 2015). Positive Matrix Factorization (PMF) was applied to the HRMS of organics using the
148 PMF2 algorithm (v4.2, robust mode) (Paatero and Tapper, 1994). The HRMS and corresponding error matrices
149 from PIKA were analyzed using the PMF Evaluation Tool v2.05 (Ulbrich et al., 2009). Data pretreatment followed
150 established protocols (Ulbrich et al., 2009; Zhang et al., 2011).
151 A six-factor solution (fPeak = 0; Q/Q_expected = 3.56) was selected as optimal (Fig. S1). The resolved OA sources
152 included hydrocarbon-like OA (HOA; 14%; O:C = 0.13), cooking-related OA (COA; 21%; O:C = 0.18), nitrogen-
153 enriched OA (NOA; 2%; O:C = 0.22), biomass-burning OA (BBOA; 13%; O:C = 0.25), less-oxidized oxygenated
154 OA (LO-OOA; 30%; O:C = 0.68), and more-oxidized oxygenated OA (MO-OOA; 20%; O:C = 1.15) (Figs. S2 and
155 S3). Alternative five- and seven-factor solutions were also evaluated. In the five-factor solution, the biomass
156 burning source was not clearly resolved and appeared to be distributed across multiple factors. In the seven-factor
157 solution, BBOA was further split into two separate factors without clear distinction or added interpretive value,
158 making the six-factor solution the most physically meaningful and interpretable (Figs. S4 and S5).
159

Formatted: Font: (Default) +Headings (Times New Roman)
11 pt

Formatted: Font: (Default) +Headings (Times New Roman)

160 2.3.2 Thermogram and Volatility Estimation

161 The chemical composition dependent mass fraction remaining (MFR) was derived at each TD temperature by
162 dividing the corrected mass concentration of the TD line [p] by the average of the adjacent bypass lines [p-1] and
163 [p+1]. Thermograms were corrected for particle loss, estimated using reference substances like NaCl, which exhibit
164 minimal evaporation (Huffman et al., 2009; Saha et al., 2014; Kang et al., 2023). OA factor concentrations at each
165 TD temperature were derived via multivariate linear regression between post-TD HRMS and ambient OA factor
166 HRMS profiles as described in Zhou et al., 2016.
167 Volatility distributions were modeled using the thermodenuder mass transfer model from Riipinen et al. (2010) and
168 Karnezi et al. (2014), implemented in Igor Pro 9 (Kang et al., 2022). OA mass was distributed into eight logarithmic
169 saturation concentration bins (C^* : 1000 to $0.0001 \mu\text{g m}^{-3}$). Modeled MFRs were fit to observations using Igor's
170 "FuncFit" function, repeated 1,000 times per OA factor to determine best-fit results. The model assumes no thermal
171 decomposition and includes adjustable parameters: mass accommodation coefficient (α_m) and enthalpy of
172 vaporization (ΔH_{exp}), randomly sampled within literature-based ranges (Table S1).
173

174 3 Results and discussion

175 **3.1 Overview of PM₁ Composition and OA Sources**

176 We conducted continuous measurements from 28 November to 28 December 2019, characterizing a winter period
177 with a mean PM₁ concentration of $27.8 \pm 15.3 \mu\text{gm}^{-3}$. This concentration is characterized as moderate; it closely
178 matches historical winter PM₁ means in Seoul (Kim et al., 2017) and implies an equivalent PM_{2.5} concentration is
179 about $34.8 \mu\text{gm}^{-3}$ (using a Korea-specific PM₁/PM_{2.5} ≈ 0.8 (Kwon et al., 2023), which is near the national 24-h PM_{2.5}
180 standard ($35 \mu\text{gm}^{-3}$) (AirKorea). The full co-evolution of PM₁, gaseous pollutants, and meteorological conditions
181 is provided in Fig. S6, showing an average ambient temperature of $1.76 \pm 4.3^\circ\text{C}$ and average relative humidity (RH)
182 of $56.9 \pm 17.5\%$ during the study.

Formatted: Font color: Auto

Formatted: Font: Not Bold, Font color: Auto

Formatted: Font color: Auto

Formatted: Font color: Auto

183 The time series of submicron aerosol (PM₁ = NR-PM₁ + BC) mass concentrations measured by the AMS (non-
184 refractory species) and MAAP (black carbon) are shown in Fig. S6, along with gaseous pollutants such as CO, SO₂,
185 and O_x (O_x = O₃ + NO₂), and meteorological parameters including relative humidity (RH), temperature, wind
186 direction, and wind speed. The mean PM₁ concentration during the study period was moderate, at $27.8 \pm 15.3 \mu\text{g}$
187 m⁻³.

188 Figure 1 summarizes the overall non-refractory submicron aerosol (NR-PM1) composition and the identified OA
189 factors. Organics (41%) and nitrate (30%) were the most abundant chemical components of PM₁, followed by
190 ammonium (12%), sulfate (10%), BC (5%), and chloride (3%) (Fig. 1a). Among the organic aerosols, six OA
191 factors were identified during the winter of 2019: hydrocarbon-like OA (HOA; 14%; O:C = 0.13), cooking-related
192 OA (COA; 21%; O:C = 0.18), nitrogen-enriched OA (NOA; 2%; O:C = 0.22), biomass burning OA (BBOA; 13%;
193 O:C = 0.25), and two types of secondary organic aerosols—less-oxidized oxygenated OA (LO-OOA; 30%; O:C =
194 0.68) and more-oxidized oxygenated OA (MO-OOA; 20%; O:C = 1.15) (Fig. 1e and Fig. S2). These compositions
195 are consistent with previous wintertime observations in Kim et al. (2017), with the exception of NOA, which will
196 be discussed in detail in Section 3.1.1.

Formatted: Font: 11 pt, Not Bold

197 PM₁ mass concentrations varied widely, ranging from 4.61 to $91.4 \mu\text{g m}^{-3}$, largely due to two severe haze episodes
198 that occurred between December 7–12 and December 22–26 (Fig. 1). During these episodes, average
199 concentrations increased significantly, driven primarily by elevated levels of nitrate, MO-OOA, and NOA (Fig.
200 1f,g). These results suggest that the haze events were caused by local accumulation of emissions and enhanced
201 SOA formation under stagnant meteorological conditions. Back-trajectory clustering shows frequent short-range
202 recirculation over the Seoul Metropolitan Area during haze (Cluster 1; Fig. S8), and the time series indicates

Formatted: Font: 11 pt, Not Bold

203 persistently low surface wind speeds during these periods (1.73 ± 0.89 vs. 2.34 ± 1.18 (clean)) (Fig. S6), together
204 pointing to stagnation-driven accumulation of local emissions; the concurrent increases in MO-OOA and NOA are
205 therefore consistent with enhanced in-city formation under stagnant conditions. Such haze episodes, characterized
206 by local emission buildup and secondary aerosol production, are a typical wintertime feature, as also reported in
207 Kim et al. (2017).

Formatted: Font: Not Bold, Font color: Auto

Formatted: Font: 11 pt, Not Bold

208 3.1.1 Nitrogen-containing organic aerosol (NOA)

209 Unlike previous wintertime aerosol studies in Seoul, this study successfully resolved a nitrogen-containing organic
210 aerosol (NOA) factor by applying positive matrix factorization (PMF) to high-resolution AMS data. NOA
211 contributed approximately 2% of the total organic aerosol (OA) mass—comparable to urban observations in
212 Guangzhou (3%; Chen et al., 2021), Pasadena (5%; Hayes et al., 2013), and New York (5.8%; Sun et al., 2011).

213 Detection of particulate NOA using real time measurement has been challenging due to its low concentration and
214 high volatility. Although Baek et al. (2022) identified nitrogen-containing species in Seoul via year-round filter-
215 based molecular analysis, PMF-based resolution of NOA in real time has not been previously reported. The
216 successful identification in this study is likely attributable to favorable winter meteorological conditions—
217 specifically low temperatures (-0.24°C) and persistently high relative humidity (~57%) compared to the 2017
218 winter season (Kim et al., 2017)—that enhanced gas-to-particle partitioning of semi-volatile amines, thereby
219 enabling their detection (Fig. S2). NOA concentrations frequently exceeded $1 \mu\text{g m}^{-3}$ when RH surpassed 60% (Fig.
220 2), supporting the importance of RH-driven partitioning and the subsequent formation of low-volatility aminium
221 salts (Rovelli et al., 2017). Although extremely low temperatures may inhibit NOA formation due to the transition
222 of aerosol particles into solid phase (Ge et al., 2011; Srivastava et al., 2022), the combination of consistently cold
223 and humid conditions during the measurement period likely promoted the partitioning of semi-volatile amines into
224 the particle phase.

Formatted: Font: Not Bold

225 In addition, episodic haze events further elevated NOA levels, increasing its contribution to OA from 1% during
226 clean periods to as much as 3% (Fig. 1f–h). These high-concentration events likely improved the signal-to-noise
227 ratio, facilitating PMF resolution. Back-trajectory analysis linked these events to regional recirculation patterns
228 (Cluster 1, Fig. S7), suggesting a predominantly local origin—consistent with the short atmospheric lifetimes and
229 high reactivity of most amines (Ge et al., 2011; Nielsen et al., 2012; Hanson et al., 2014).

Formatted: Font: (Default) Times New Roman

Formatted: Justified, Line spacing: 1.5 lines

Formatted: Font: (Default) Times New Roman, 11 pt

The NOA factor exhibited the highest nitrogen-to-carbon (N:C) ratio (0.22) and the lowest oxygen-to-carbon (O:C) ratio (0.19) among all POA factors (Fig. S2), indicating a chemically reduced, nitrogen-rich composition. The factor represents semi-volatile, reduced nitrogen species that originate from primary urban combustion sources but whose observed mass in the particle phase is enhanced by rapid secondary partitioning and salt formation (Ge et al., 2011; You et al., 2014). The NOA mass spectrum was dominated by amine-related fragments including m/z 30 (CH_3N^+), 44 ($\text{C}_2\text{H}_5\text{N}^+$), 58 ($\text{C}_3\text{H}_8\text{N}^+$), and 86 ($\text{C}_5\text{H}_{12}\text{N}^+$) (Fig. 3a). The spectral signature of the factor is defined by the characteristic dominance of the m/z 44 fragment, which typically serves as the primary marker for dimethylamine (DMA)-related species, closely followed by m/z 58 (trimethylamine, TMA) and m/z 30 (methylamine, MA). This profile is in strong agreement with NOA factors resolved via PMF in other polluted environments. For instance, the dominance of m/z 44 and m/z 30 aligns with amine factors reported in New York City (Sun et al., 2011) and Pasadena, California (Hayes et al., 2013). This DMA-dominated signature is also consistent with seasonal characterization of organic nitrogen in Beijing (Xu et al., 2017) and Po Valley, Italy (Saarikoski et al., 2012), reinforcing the common chemical signature of reduced organic nitrogen across diverse urban and regional environments. Furthermore, the presence of non-negligible signals at m/z 58 and m/z 86 supports the contribution of slightly larger alkylamines, a pattern that aligns well with established AMS laboratory reference spectra for these reduced nitrogen compounds (Ge et al., 2011; Silva et al., 2008).

246 These amines are commonly emitted during the combustion of nitrogen-rich biomass and proteinaceous materials
247 and are frequently associated with biomass-burning emissions (Ge et al., 2011). Previous molecular analyses in
248 Seoul also indicate DMA, MA, and TMA as the dominant amine species in December (Baek et al., 2022). While
249 other amines such as triethylamine (TEA), diethylamine (DEA), and ethylamine (EA) may contribute via
250 industrial/solvent pathways (e.g., chemical manufacturing, petrochemical corridors, wastewater treatment), our
251 HR-AMS spectra are dominated by small alkylamine fragments (m/z 30, 44, 58, 86) and the diurnal behavior co-
252 varies with combustion markers (below), indicating a primarily combustion-linked influence. Nevertheless, recent
253 urban measurements and sector-based analyses show that industrial activities can contribute measurable amines in
254 cities (Tiszenkel et al., 2024; Zheng et al., 2015; Mao et al., 2018; Shen et al., 2017; Yao et al., 2016). Accordingly,
255 a minor NOA contribution from solvent/industrial amines cannot be excluded.

256 The NOA factor exhibited the highest nitrogen to carbon (N:C) ratio (0.22) and the lowest oxygen to carbon (O:C) 257 ratio (0.19) among all POA factors (Fig. S2), indicating a chemically reduced, nitrogen-rich composition. Its mass 258 spectrum was dominated by amine-related fragments, including m/z 20 (CH_2N^+), 44 ($\text{C}_2\text{H}_5\text{N}^+$), 58, and 86 (Fig. 3a).

Formatted: Font: (Default) Times New Roman, 11 pt, Not Bold
Formatted: Font: (Default) Times New Roman, 11 pt
Formatted: Font color: Auto
Formatted: Font: (Default) Times New Roman, 11 pt
Formatted: Font: (Default) Times New Roman, 11 pt
Formatted: Font: (Default) Times New Roman, 11 pt, Not Bold, Italic
Formatted: Font: (Default) Times New Roman, 11 pt, Not Bold
Formatted: Font: (Default) Times New Roman, 11 pt, Not Bold, Subscript
Formatted
Formatted: Font: (Default) Times New Roman, 11 pt
Formatted
Formatted: Font: (Default) Times New Roman, 11 pt
Formatted: Font: (Default) Times New Roman, 11 pt, Italic
Formatted: Font: (Default) Times New Roman, 11 pt
Formatted: Font: (Default) Times New Roman, Not Bold
Formatted: Font: Italic

259 closely matching reference spectra of low molecular weight alkylamines such as dimethylamine (DMA),
260 trimethylamine (TMA), methylamine (MA), and dibutylamine (DBA) (Fig. 3b-e). These amines are commonly
261 emitted during the combustion of nitrogen rich biomass and proteinaceous materials and are frequently associated
262 with biomass burning emissions (Ge et al., 2011). While other amines like triethylamine (TEA), diethylamine
263 (DEA), and ethylamine (EA) may contribute, their typical sources—such as industrial processes, solvent use, or
264 wastewater treatment (E. Poste et al., 2014; He et al., 2016; Ge et al., 2011)—are distinct from biomass combustion,
265 and thus they are considered less likely to be the dominant contributors under wintertime conditions in Seoul.
266 Previous molecular analysis by Baek et al. (2022) also supports DMA, MA, and TMA as the main amine species
267 observed during December in Seoul.

268 Supporting this, NOA exhibited a diurnal pattern similar to that of BBOA, with both peaking at night and in the
269 early morning (Fig. 2a), suggesting shared sources or formation mechanisms. Biomass burning under cold, oxygen-
270 limited conditions is known to emit various amines and amides (You et al., 2014; Yao et al., 2016), which may
271 contribute directly to NOA or serve as precursors for its secondary formation. Strong correlations with CH_4N^+ ($r = 0.95$) and $\text{C}_2\text{H}_6\text{N}^+$ ($r = 0.91$) (Fig. 2) further support the presence of reduced nitrogen compounds, typically
272 associated with residential fuel combustion and wintertime heating. However, the time series of NOA and BBOA
273 were not well correlated (Fig. 2 and S7), likely because NOA episodes preferentially occurred during haze periods
274 under stagnant conditions (Fig. 1), whereas BBOA emissions tend to follow a more regular, daily emission pattern.
275 Under cold, humid, and stagnant conditions, these semi-volatile amines can readily partition into the particle phase
276 and form low-volatility aminium salts, enhancing the observed NOA signal. Taken together, these results suggest
277 that NOA during wintertime in Seoul is strongly influenced by a combination of combustion-related primary
278 emissions and subsequent atmospheric processing of amine-containing species, facilitated by seasonally favorable
279 conditions.

Formatted: Font: 11 pt

281 3.1.2 Secondary organic aerosols (SOA)

282 In this study, two oxygenated organic aerosol (OOA) factors—more-oxidized OOA (MO-OOA) and less-oxidized
283 OOA (LO-OOA)—were identified, together accounting for approximately half of the total organic aerosol (OA)
284 mass. This fraction is notably higher than that reported in previous wintertime urban studies (Kim et al., 2017;
285 Zhang et al., 2007). Both OOA factors exhibited characteristic mass spectral features, including prominent peaks at m/z
286 44 (CO_2^+) and m/z 43 ($\text{C}_2\text{H}_3\text{O}^+$), which are widely recognized as markers of oxygenated organics (Fig. S2e, S3f).
287 The oxygen-to-carbon (O:C) ratios for MO-OOA and LO-OOA were 1.15 and 0.68, respectively, indicating highly

Formatted: Font: Italic

Formatted: Font: Italic

288 oxidized chemical compositions. The O:C ratio of MO-OOA was especially elevated, exceeding those reported in
289 previous Seoul campaigns—0.68 in winter 2015 (Kim et al., 2017), 0.99 in spring 2019 (Kim et al., 2020), and
290 0.78 in fall 2019 (Jeon et al., 2023)—while the LO-OOA ratio was within a similar range.

291 MO-OOA showed strong correlations with secondary inorganic species such as nitrate ($r = 0.90$), ammonium ($r = 0.92$), and sulfate ($r = 0.81$), consistent with its formation through regional and local photochemical aging processes
292 (Fig. S3). **In contrast, LO-OOA exhibited only modest correlations with sulfate, nitrate, and ammonium ($r = 0.50$,**
293 **0.51, and 0.42, respectively**, suggesting additional contributions from semi-primary sources not closely linked to
294 **inorganic secondary formation (e.g., cooking, traffic, biomass burning)**). In contrast, LO-OOA exhibited only
295 **moderate correlations with these inorganics ($r = 0.50$, 0.51 , and 0.42 , respectively)**, which may suggest an
296 **additional influence from other semi-primary sources not strongly associated with inorganic secondary species**
297 **such as biomass burning.** LO-OOA does not exhibit a pronounced m/z 60 (levoglucosan) signal (Fig. S2); however,
298 **the levoglucosan marker (f_{60}) is known to diminish with atmospheric aging and can become weak or undetectable**
299 **downwind (Hennigan et al., 2010; Cubison et al., 2011).** Taken together, the weaker coupling with secondary
300 **inorganics and the absence of a strong m/z 60 peak indicate that LO-OOA is a mixture of aged secondary organics**
301 **and semi-primary urban emissions, while a contribution from aged biomass-burning influence cannot be ruled**
302 **out.** This interpretation is further supported by a minor signal at m/z 60—indicative of levoglucosan, a known tracer
303 **for biomass burning (Fig. S2).** The weaker coupling with secondary inorganics implies that LO-OOA may represent
304 **a mixture of aged and semi-primary organics, partially derived from combustion-related activities.**

306 3.1.3 Primary organic aerosols (POA)

307 Three primary organic aerosol (POA) factors were identified in this study: hydrocarbon-like OA (HOA), cooking-
308 related OA (COA), and biomass burning OA (BBOA). These three components exhibited mass spectral and
309 temporal characteristics consistent with previous observations in Seoul and other urban environments. HOA was
310 characterized by dominant alkyl fragment ions ($C_nH_{2n+1}^+$ and $C_nH_{2n-1}^+$; Fig. S2a) and a low O:C ratio (0.13),
311 consistent with traffic-related emissions (0.05–0.25) (Canagaratna et al., 2015). It showed strong correlations with
312 vehicle-related ions $C_3H_7^+$ ($r = 0.79$) and $C_4H_9^+$ ($r = 0.86$) (Kim et al., 2017; Canagaratna et al., 2004; Zhang et al.,

Formatted: Normal, Space Before: Auto, After: Auto, Line spacing: single

Formatted: Font: 11 pt, Font color: Auto

Formatted: Font color: Auto

Formatted: Font: 11 pt, Font color: Auto

313 2005), and exhibited a distinct morning rush hour peak (06:00–08:00), followed by a decrease likely driven by
314 boundary layer expansion (Fig. S3a).

315 COA, accounting for 21% of OA, showed higher contributions from oxygenated ions than HOA, with tracer peaks
316 at m/z 55, 84 and 98 (Fig. S2b) consistent with cooking emissions (Sun et al., 2011). It correlated strongly with
317 cooking-related ions such as $C_3H_9O^+$ ($r = 0.94$), $C_5H_8O^+$ ($r = 0.96$), and $C_6H_{10}O^+$ ($r = 0.98$) (Fig. S3h), and displayed
318 prominent peaks during lunch and dinner hours, reflecting typical cooking activity patterns.

Formatted: Font: Italic

319 BBOA was identified based on characteristic ions at m/z 60 ($C_2H_4O_2^+$) and 73 ($C_3H_5O^+$), both of which are
320 associated with levoglucosan—a well-established tracer for biomass burning (Simoneit et al., 2002). Its relatively
321 high f_{60} and low f_{44} values (Fig. S8a) indicate that the BBOA observed in this study was relatively fresh and had
322 not undergone extensive atmospheric aging (Cubison et al., 2011). Furthermore, BBOA exhibited moderate
323 correlations with NOA in both diurnal profiles and time series (Fig. 2), particularly with nitrogen-containing ions
324 such as $C_2H_4N^+$ ($r = 0.67$) and $C_2H_6N^+$ ($r = 0.56$) (Fig. 2 and S3), which are also dominant peaks in the NOA mass
325 spectrum. This overlap suggests a potential shared emission source or co-emission scenario, ~~such as biomass~~
326 ~~burning, which is known consistent with the co-emission of to emit~~ both organic aerosols and reduced nitrogen-
327 containing compounds. ~~Regarding source location, several pathways can influence Seoul's biomass burning~~
328 ~~signature. First, urban/peri-urban small-scale burning (e.g., solid-fuel use in select households, restaurant charcoal~~
329 ~~use, and intermittent waste burning) has been reported and can enhance BBOA locally (Kim et al., 2017). Second,~~
330 ~~nearby agricultural-residue burning in surrounding provinces occurs seasonally and can episodically impact the~~
331 ~~metropolitan area (Han et al., 2022). Third, regional transport from upwind regions (e.g., northeastern China/North~~
332 ~~Korea) can bring biomass burning influenced air masses under northerly/northwesterly flow (Lamb et al., 2018;~~
333 ~~Nault et al., 2018). In this dataset, the nighttime and early-morning enhancements, the BBOA–NOA co-variation,~~
334 ~~and trajectory clusters showing regional recirculation indicate a predominantly local/near-source contribution~~
335 ~~during the study period (Yoo et al., 2024), with episodic non-local influences remaining possible.~~

Formatted: Font: Italic

Formatted: Font: Italic

Formatted: Font: Italic

Formatted: Font: Not Bold, Font color: Auto

Formatted: Font color: Auto

336 3.2 Volatility of Non-Refractory Species

337 Figure 4 presents thermograms of non-refractory (NR) species measured by HR-ToF-AMS. The mass fraction
338 remaining (MFR) after thermodenuder (TD) treatment follows the typical volatility trend reported in previous
339 studies (Xu et al., 2016; Kang et al., 2022; Jeon et al., 2023; Huffman et al., 2009): nitrate was the most volatile,
340 followed by chloride, ammonium, organics, and sulfate. Nitrate showed the steepest decline with temperature, with

341 a T_{50} of ~ 67 °C—higher than pure ammonium nitrate (~ 37 °C; Huffman et al., 2009), suggesting contributions from
342 less volatile species like organonitrates or metal nitrates (Feng et al., 2023). Nearly complete evaporation occurred
343 by 200 °C (~2% remaining). Compared to previously reported fall conditions ($T_{50} \sim 73$ °C, incomplete evaporation),
344 winter nitrate appeared more volatile, indicating relatively fewer non-volatile nitrate forms (e.g., Kang et al., 2022;
345 Jeon et al., 2023). Compared to fall ($T_{50} \sim 73$ °C, incomplete evaporation), winter nitrate appeared more volatile,
346 supporting enhanced NOA detection and indicating relatively fewer non-volatile nitrate forms. Sulfate was the least
347 volatile ($T_{50} \approx 170$ °C), consistent with ammonium sulfate (Scott and Cattell, 1979). A subtle slope change near
348 140 °C likely reflects ammonium-sulfate morphology/phase-state changes and/or organosulfate–inorganic mixing,
349 rather than contributions from metallic (refractory) sulfates, which are not efficiently detected by AMS. ~~Sulfate was~~
350 ~~the least volatile ($T_{50} \sim 170$ °C), consistent with ammonium sulfate (Scott and Cattell, 1979). A subtle slope change~~
351 ~~near 140 °C may suggest phase transitions or less volatile sulfate components.~~ About 25% remained at 200 °C,
352 indicating possible contributions from metallic or organic sulfates. Ammonium showed intermediate volatility,
353 with T_{50} between nitrate and sulfate. Its slightly lower winter T_{50} suggests stronger nitrate association. Residual
354 ammonium at 200 °C was consistent (~4%) in previously reported spring/fall measurements (Kang et al., 2022;
355 Jeon et al., 2023). Residual ammonium at 200 °C was consistent (~4%) across seasons (Kang et al., 2022; Jeon et
356 al., 2023). Chloride volatility was also comparable across seasons in prior studies in terms of T_{50} , but exhibited
357 more complete evaporation in winter (~4% residual vs. ~10% in fall), possibly reflecting a shift in source to more
358 volatile forms like road salt during wintertime. Chloride volatility was also comparable between seasons in terms
359 of T_{50} , but exhibited more complete evaporation in winter (~4% residual vs. ~10% in fall), possibly reflecting a
360 shift in source to more volatile forms like road salt during wintertime.

361 Organic aerosol (OA) exhibited moderate volatility ($T_{50} \sim 120$ °C), consistent with the presence of a wide variety
362 of compounds with differing volatilities. This trend aligns with previously reported spring and fall observations in Seoul,
363 Korea (Kang et al., 2022; Jeon et al., 2023). This trend aligns with spring and fall observations (Kang et al., 2022; Jeon
364 et al., 2023).

365 3.2.1 Volatility Profiles of Organic sources

366 Figure 5 presents the volatility distributions of six OA sources within the volatility basis set (VBS) framework.
367 Volatility is expressed as the effective saturation concentration (C^* , $\mu\text{g m}^{-3}$), where higher C^* values correspond
368 to higher volatility. Following Donahue et al. (2009), C^* values are categorized into four bins: extremely low-
369 volatility organic compounds (ELVOCs, $\log C^* < -4.5$), low-volatility organic compounds (LVOCs, $-4.5 < \log$

Formatted: Font: 10 pt

370 $C^* < -0.5$), semi-volatile organic compounds (SVOCs, $-0.5 < \log C^* < 2.5$), and intermediate-volatility organic
371 compounds (IVOCs, $2.5 < \log C^* < 6.5$).

372 Among the primary OA (POA) sources, hydrocarbon-like OA (HOA) exhibited the highest volatility, with mass
373 predominantly distributed in the SVOC and IVOC ranges. This is consistent with its low oxidation state (O:C =
374 0.35) and primary emission characteristics. Mass fraction remaining (MFR) results (Fig. S9) further support this,
375 showing rapid mass loss at lower temperatures. Biomass burning OA (BBOA) and nitrogen-containing OA (NOA)
376 also showed high volatility, peaking in the SVOC–IVOC range ($\log C^* = 1–3$), and had lower O:C ratios of 0.25
377 and 0.19, respectively. Their slightly more oxidized nature relative to HOA, despite a similar volatility range, may
378 reflect emissions occurring under nighttime or cooler conditions, which promote condensation of otherwise volatile
379 species. The similar volatility distributions and MFR profiles of BBOA and NOA (Fig. S9) further support the
380 possibility of a shared emission source or formation pathway (Section 3.1.1). Cooking-related OA (COA) showed
381 a more moderate volatility profile, with mass more evenly distributed across the LVOC and SVOC bins. This
382 pattern reflects its diverse cooking sources and variable emission profiles as previously reported (Kang et al.,
383 2022). This pattern reflects its diverse cooking sources and variable emission profiles (Kang et al., 2022).

384 For secondary OA (SOA), less-oxidized oxygenated OA (LO-OOA) exhibited the lowest volatility, with substantial
385 mass in the LVOC and ELVOC bins ($C^* \approx 10^{-3}–10^{-4}$), consistent with its aged, highly condensed nature. This is in
386 agreement with previous findings in Seoul during spring (Kang et al., 2022). In contrast, more-oxidized OOA (MO-
387 OOA), despite its higher oxidation state (O:C = 1.15), displayed greater volatility, with a peak at $C^* \approx 10^1$. This
388 discrepancy likely reflects differences in formation and aging processes, as discussed further in Section 3.2.53.

389 Overall, the volatility characteristics across OA factors suggest that oxidation state alone does not fully explain
390 volatility. Rather, volatility is shaped by a combination of emission source, emission timing, temperature, and
391 atmospheric processing. These findings highlight the importance of integrating both chemical and physical
392 characterization to better understand OA formation and aging across seasons.

393 **3.3 Aging effect on volatility from 2D VBS**

394 Generally, the oxygen-to-carbon (O:C) ratio of organic aerosols (OA) is inversely related to their volatility. As O:C
395 increases through aging, the effective saturation concentration (C^*) typically decreases, resulting in lower volatility
396 (Donahue et al., 2006; Jimenez et al., 2009). This common relationship arises because the addition of oxygen-
397 containing functional groups (e.g., hydroxyl, carboxyl, carbonyl), which increases molecular weight and enhances

398 intermolecular interactions such as hydrogen bonding, thereby reducing vapor pressure (Jimenez et al., 2009; Kroll
399 and Seinfeld, 2008). Moreover, oxidative aging often leads to oligomerization or functionalization, promoting
400 particle-phase retention and reducing the effective saturation concentration (C*) (Donahue et al., 2011; Robinson
401 et al., 2007).

402 However, in this study, the most oxidized OA factor—MO-OOA, with a ~~an~~ high O:C ratio of 1.15—exhibited
403 unexpectedly high volatility. Its volatility distribution was skewed toward SVOCs and IVOCs (Fig. 5), and its rapid
404 mass loss in MFR thermograms (Fig. S9) further indicated low thermal stability. This observation appears to
405 contradict the usual inverse O:C–volatility relationship; however, under winter haze conditions—with suppressed
406 O_x/low OH, particle-phase autoxidation and fragmentation can yield higher-O:C yet more volatile products, with
407 enhanced condensation on abundant particle surface area (details below).

408 Viewed against prior TD-AMS results, the volatility of Seoul's winter MO-OOA presents a unique case,
409 particularly in the nature of its O:C-volatility relationship. Prior urban studies have commonly reported substantial
410 SVOC-OA, consistent with high photochemical activity or elevated loadings; for example, Mexico City/Los
411 Angeles showed pronounced SVOC–IVOC contributions during warm seasons (Cappa and Jimenez, 2010), and
412 summertime Beijing and wintertime Shenzhen likewise exhibited strong overall OA volatility (Xu et al., 2019; Cao
413 et al., 2018). While these comparisons establish that volatile OA is common, they generally did not report the
414 factor-level inversion observed here, where the highly-oxidized OOA component (MO-OOA) was more volatile
415 than a less-oxidized OOA (LO-OOA). This behavior is distinct from findings in colder, lower-loading regimes;
416 wintertime Paris, for instance, maintained the conventional hierarchy where the more-oxidized OOA was
417 comparatively less volatile (Paciga et al., 2016). Furthermore, seasonal context within Seoul showed springtime
418 OA with lower oxidation levels than our winter MO-OOA despite similar SVOC contributions (Kang et al., 2022).
419 This comprehensive comparison underscores the unusual nature of the O:C-volatility relationship observed under
420 the specific winter haze conditions in Seoul.

421

422 3.3.1 Proposed Mechanism: Fragmentation and Condensation under Low-OH Haze

Formatted: Font: 11 pt

Formatted: Font: 11 pt, Not Italic

Formatted: Font: 11 pt

Formatted: Font: 11 pt

423 This observation appears to contradict the expected inverse relationship between O:C and volatility but may be
424 explained by alternative oxidation mechanisms and specific environmental conditions.

425 MO-OOA concentrations increased during haze episodes—characterized by reduced ozone levels, low solar
426 radiation and elevated aerosol mass concentrations (Fig. 6 and Fig. S6, yellow shading). The suppressed ozone
427 likely indicates lower OH radical production via O_3 photolysis, leading to a low-OH oxidation regime. We note
428 that haze also suppresses HONO photolysis; however, HONO concentrations can be elevated at night and early
429 morning via heterogeneous NO_2 conversion and surface emissions, so net OH from HONO may remain non-
430 negligible even as photolysis rates are depressed (e.g., Gil et al., 2021; Kim et al., 2024; Slater et al., 2020). Under
431 such conditions, particle-phase autoxidation involving RO_2 radicals can become the dominant oxidation pathway.

432 Even under low-OH conditions, NO_3 formed via $NO_2 + O_3$ can initiate RO_2 production through addition to alkenes,
433 while reduced photolysis at night/low light extends NO_3 lifetimes; these RO_2 then participate in particle-phase
434 autoxidation, yielding highly oxygenated yet relatively volatile products. These processes tend to produce highly
435 oxidized but relatively low-molecular-weight products (Ehn et al., 2014; Zhao et al., 2023). Unlike classical OH-
436 initiated, multi-generational aging—which increases molecular mass and reduces volatility—fragmentation-
437 dominated oxidation can cleave larger precursors into smaller oxygenated compounds, resulting in higher volatility
438 despite elevated O:C. Consistent with this interpretation, online AMS/FIGAERO-CIMS and EESI-TOF, as well as
439 offline HRMS/GC-MS, have reported high-O:C yet more-volatile product distributions accompanied by elevated f_{44}
440 with comparatively stable f_{44} under fragmentation-dominated aging (Kroll et al., 2009; Ng et al., 2010; Chhabra et
441 al., 2011; Lambe et al., 2012; Lopez-Hilfiker et al., 2016; D'Ambro et al., 2017). Furthermore, high aerosol mass
442 loadings during haze events provide abundant surface area for the uptake of semi-volatile/intermediate-volatility
443 organics via absorptive partitioning, so that higher CO_A enhances condensation (Pankow, 1994; Donahue et al.,
444 2006; Hallquist et al., 2009; Robinson et al., 2007). We also note that functionalized, low-molecular-weight
445 compounds can reside in the SVOC-IVOC range and thus contribute to the high apparent volatility of MO-OOA
446 (Ng et al., 2010; Chhabra et al., 2011; Lopez-Hilfiker et al., 2016; D'Ambro et al., 2017). species. This facilitates
447 the condensation of even relatively volatile, oxidized compounds onto particles (Fig. 6). The net result is an
448 apparent increase in both oxidation state and volatility of OA, as reported in aging studies under stagnant and
449 polluted conditions (Jimenez et al., 2009; Ng et al., 2016).

450 In line with these reports, our results also revealed a decoupling between O:C and volatility, with MO-OOA
451 showing high volatility despite its elevated O:C ratio (~1.15). While this behavior has been observed in other urban

Formatted: Font: Not Bold, Font color: Auto

Formatted: Font color: Auto

Formatted: Font color: Auto

Formatted: Font: 11 pt, Font color: Auto

Formatted: Font color: Auto

Formatted: Font: 11 pt, Font color: Auto

Formatted: Font color: Auto

Formatted: Font: Not Bold, Font color: Auto

Formatted: Font: 11 pt, Not Bold, Font color: Auto

Formatted: Font: 11 pt, Font color: Auto

Formatted: Font color: Auto

452 environments, this study provides one of the first detailed thermodynamic assessments of this decoupling under
453 winter haze conditions in Seoul using real-time TD-AMS measurements. Supporting this interpretation, MO-OOA
454 in this study was characterized by a consistently high f_{44} (CO_2^+) signal and a relatively stable f_{43} ($\text{C}_2\text{H}_3\text{O}^+$) signal
455 compared to LO-OOA (Fig. S8b). During specific periods when MO-OOA concentrations increased, only f_{44} was
456 noticeably enhanced, while f_{43} remained flat (Fig. 6). This temporal pattern—elevated f_{44} without corresponding
457 changes in f_{43} —is a typical signature of highly oxidized and fragmented organic aerosol and suggests advanced
458 aging dominated by fragmentation rather than functionalization (Kroll et al., 2009). Consistent with this, the haze–
459 non-haze comparison, including the high-MO-OOA interval (Fig. S12), shows larger oxygenated fragments (m/z 28, 29, 44)
460 and higher f_{44} and O:C during haze, whereas non-haze periods exhibit relatively larger fractional hydrocarbon fragments (m/z
461 41, 43, 55, 57). These spectral contrasts indicate that the elevated volatility of MO-OOA reflects advanced oxidation—via
462 autoxidation and the condensation of small oxygenated fragments—rather than enrichment of high-molecular-weight ions,
463 particularly under conditions of limited OH and high particulate surface area.

464 Thus, although MO-OOA had a high O:C ratio, its elevated volatility likely reflects oxidation dominated by
465 autoxidation, fragmentation, and condensation of small oxygenated fragments under conditions of limited OH
466 availability and high particulate surface area.

467 This unexpected volatility behavior of highly oxidized MO-OOA highlights the need for secondary organic aerosol
468 (SOA) models to incorporate fragmentation-dominated oxidation pathways—especially under haze conditions
469 where conventional assumptions linking O:C to volatility may break down. Including such mechanisms could
470 improve model accuracy in representing OA aging and volatility in urban air quality simulations.

471 4 Conclusions

472 This study offers a detailed characterization of wintertime submicron aerosols (PM_1) in Seoul by integrating
473 chemical composition, volatility behavior, and source apportionment to better understand their formation and
474 atmospheric evolution. Organic aerosols (OA), particularly secondary organic aerosols (SOA), were the dominant
475 PM_1 component, highlighting the significance of oxidative processes even during cold seasons. A notable result is
476 the successful real-time resolution of a nitrogen-containing organic aerosol (NOA) factor, enabled by cold, humid
477 meteorological conditions that enhanced the partitioning and stabilization of amine-derived compounds. The NOA
478 factor was characterized by tracer ions associated with low-molecular-weight alkylamines such as TMA, DMA,
479 and MA, which likely originated from biomass combustion.

Formatted: Font color: Auto
Formatted: Font: Not Bold, Font color: Auto
Formatted: Font: Not Bold, Italic, Font color: Auto
Formatted: Font: Not Bold, Font color: Auto
Formatted: Font: Not Bold, Italic, Font color: Auto
Formatted: Font: Not Bold, Font color: Auto

480

481 Volatility analysis revealed distinct thermodynamic behavior across OA sources. Primary OA factors such as HOA,
482 BBOA, and COA exhibited relatively high volatility, while LO-OOA showed low volatility and a higher oxidation
483 state, consistent with aged, low-volatility material. The similarity in volatility distributions and diurnal patterns
484 between BBOA and NOA suggests that biomass combustion under wintertime conditions is a likely contributor to
485 both primary organic and nitrogenous aerosol formation.

486

487 Interestingly, MO-OOA—despite its high oxygen-to-carbon (O:C) ratio—exhibited elevated volatility, diverging
488 from the expected inverse relationship between oxidation state and volatility. This suggests that under stagnant,
489 polluted conditions with suppressed ozone and OH radical levels, particle-phase autoxidation and fragmentation
490 pathways may dominate over traditional OH-initiated aging, yielding highly oxidized yet semi-volatile products.
491 These findings highlight the importance of coupling high-resolution chemical and physical aerosol measurements
492 to better understand OA formation processes and properties within urban air quality frameworks. Consequently,
493 air quality models should incorporate diverse oxidation mechanisms and avoid assuming a direct link between
494 oxidation state and volatility.

495 **Acknowledgements**

Formatted: Font color: Auto

496 This work was supported by the National Research Foundation of Korea (NRF) grant funded by the Korea government (MSIT)
497 (RS-2025-00514570), the project “development of SMaRT based aerosol measurement and analysis systems for the evaluation
498 of climate change and health risk assessment” operated by Seoul National University (900-20240101).

499 **Author Contributions**

Formatted: Font color: Auto

500 Hwajin Kim designed and prepared the manuscript. Jiwoo Jeong operated the TD-AMS and analyse the data. Jihye Moon
501 analyse the data. Hyungu Kang analyse the volatility of OA.

502 **Conflicts of Interest**

Formatted: Font color: Auto

503 Authors declare that they have no conflict of interest.

504

505

506

507

508

509

510

511

512

513

514

515

516

517

518

519

520

521

522

523

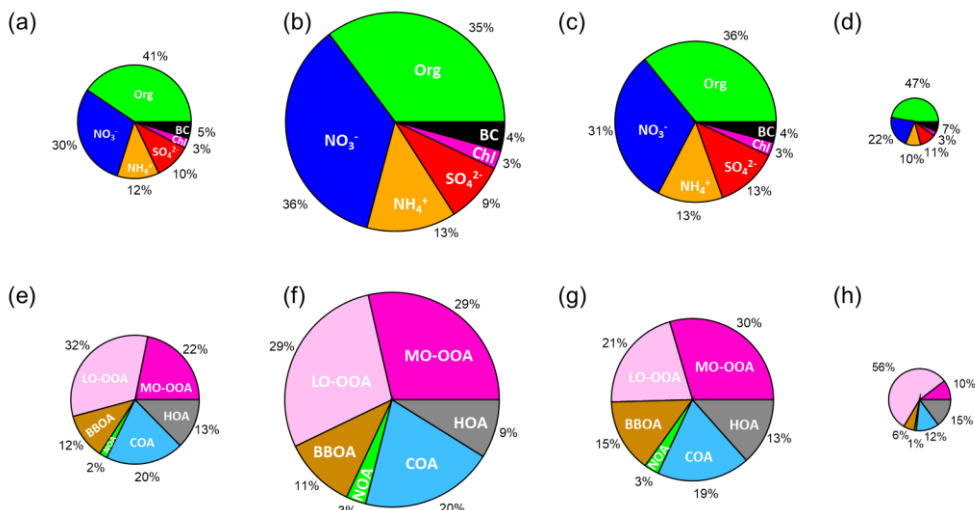
524

525 Tables and Figures

526

527

528



529

	Period	Standard	Avg. Mass conc. ($\mu\text{g m}^{-3}$)
Total	2019.11.28 ~ 2019.12.28		Avg $\text{PM}_1 = 26.37$
Clean	2019.12.04 ~ 2019.12.06	Daily $\text{PM}_1 < 10.00 \mu\text{g m}^{-3}$	Avg $\text{PM}_1 = 9.98$
Haze 1	2019.12.07 ~ 2019.12.11	Daily $\text{PM}_1 > 30.00 \mu\text{g m}^{-3}$	Avg $\text{PM}_1 = 51.88$
Haze 2	2019.12.21 ~ 2019.12.25	Daily $\text{PM}_1 > 30.00 \mu\text{g m}^{-3}$	Avg $\text{PM}_1 = 37.71$

530

531 **Figure 1.** Compositional pie charts of PM_1 species for (a) the entire study period, (b) haze period 1, (c) haze period 2, and
 532 (d) a clean period; and of each OA source for (e) the entire study period, (f) haze period 1, (g) haze period 2, and (h) the
 533 clean period. Table. Standard and average PM_1 mass concentrations during the entire study period, haze period 1, haze period
 534 2, and the clean period.

535

536

537

538

539

540

541

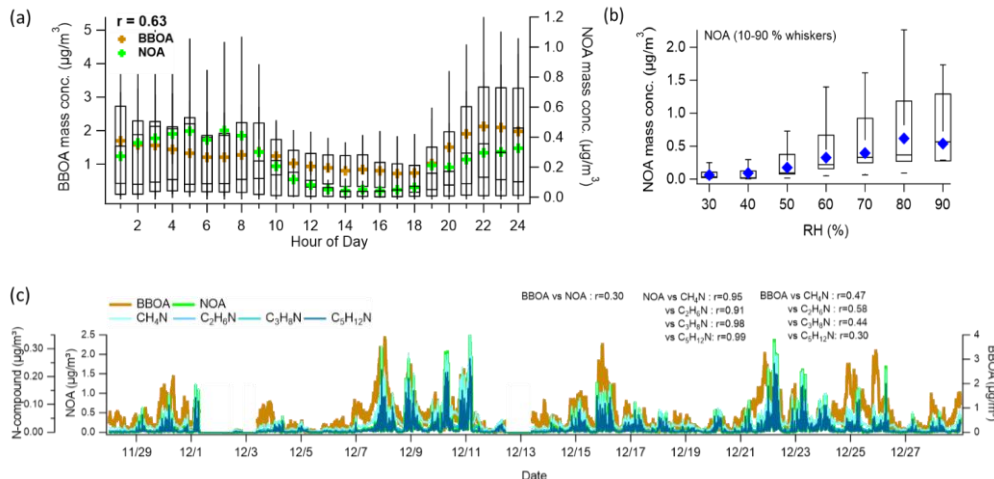
542

543

544

Formatted: Font color: Auto
Formatted: Font color: Auto

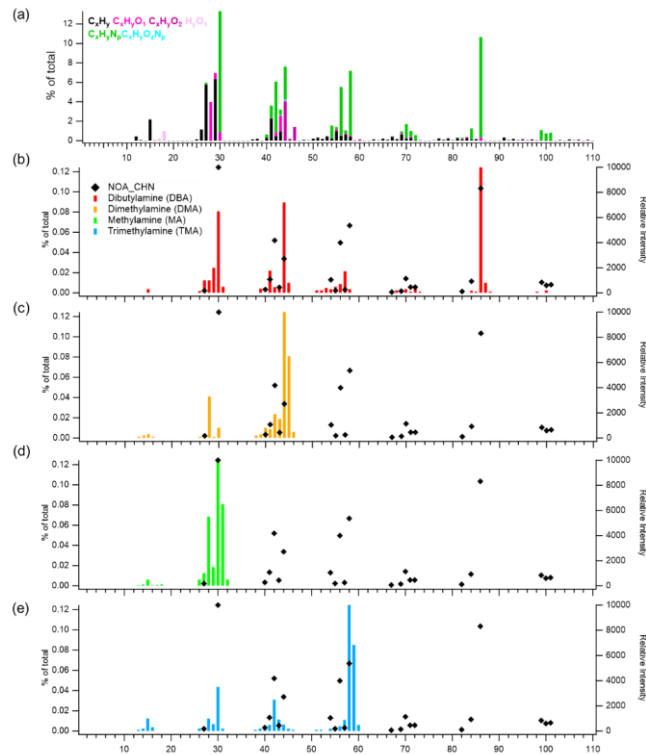
545



546

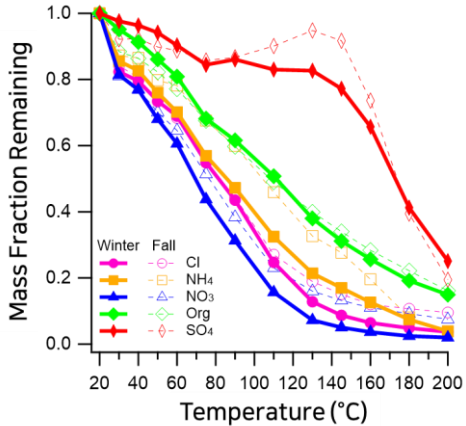
547

548 **Figure 2.** (a) Diurnal mean profiles of NOA and BBOA. Whiskers denote the 90th and 10th percentiles; box
 549 edges represent the 75th and 25th percentiles; the horizontal line indicates the median, and the colored marker
 550 shows the mean. The diurnal correlation between NOA and BBOA mean values is 0.63.
 551 (b) Relative humidity (RH)-binned nighttime (19:00–05:00) profile of NOA. Box and whisker definitions are the
 552 same as in panel (a). (c) Time series of NOA, BBOA, and amine-related ions (CH_4N^+ , $\text{C}_2\text{H}_5\text{N}^+$, $\text{C}_3\text{H}_8\text{N}^+$,
 553 $\text{C}_5\text{H}_{12}\text{N}^+$), along with their correlations with NOA and BBOA.
 554

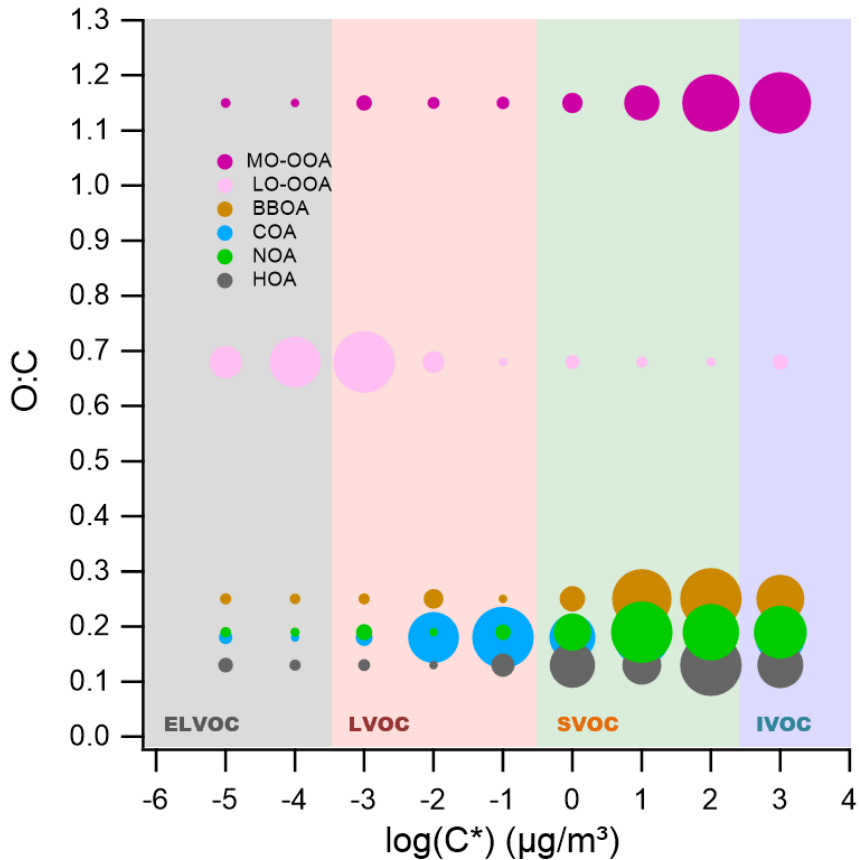


555
556 **Figure 3.** Mass spectra of (a) the NOA factor resolved by PMF analysis in this study, and reference spectra of amines from
557 the NIST library: (b) dibutylamine (DBA), (c) dimethylamine (DMA), (d) methylamine (MA), and (e) trimethylamine
558 (TMA). In panels (b)–(e), the left y-axis indicates the contribution of CHN-containing ions in the NOA factor (% of total),
559 while the right y-axis shows the relative intensity of each compound's mass spectrum from the NIST library.

560
561
562

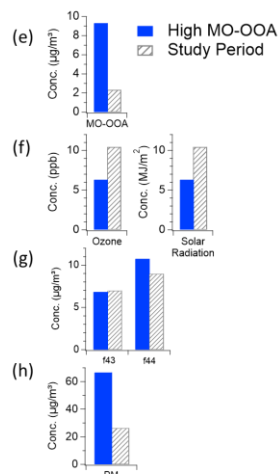
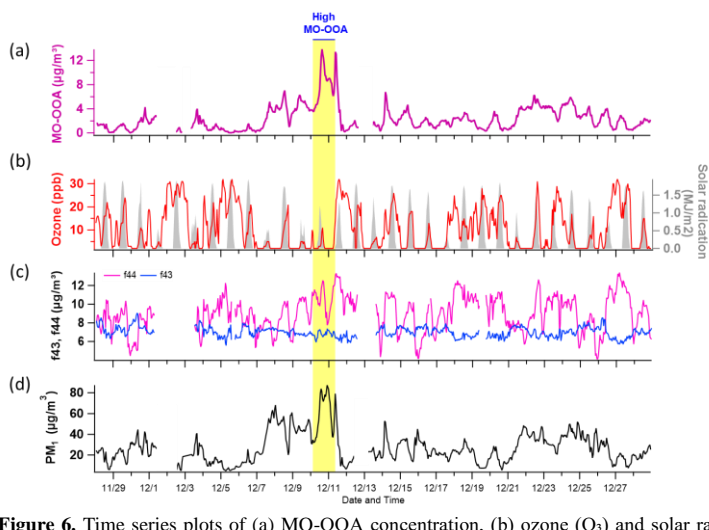


563 **Figure 4.** Mass fraction remaining (MFR) of non-refractory (NR) aerosol species measured in Seoul [during fall \(solid lines\)](#)
 564 [and winter \(dashed lines\) 2019](#) using a thermodenuder coupled to a high-resolution time-of-flight aerosol mass spectrometer
 565 [\(HR-ToF-AMS\). Winter 2019 \(this study; dashed\) is compared with fall 2019 \(previously reported; solid\) \(Jeon et al.,](#)
 566 [2023\).](#) Species include organics (magenta), nitrate (blue), sulfate (orange), ammonium (green), and chloride (red).



567
568
569 **Figure 5.** Two-dimensional volatility basis set (2D-VBS) representation of organic aerosol (OA) sources identified in winter
570 2019 in Seoul. The plot illustrates the relationship between the oxygen-to-carbon (O:C) ratio and the effective saturation
571 concentration (C^*) for each OA source resolved via positive matrix factorization (PMF). Solid circles represent the volatility
572 distribution across C^* bins, with marker size proportional to the mass fraction within each bin for the given source. Shaded
573 regions correspond to different volatility classes: extremely low-volatility organic compounds (ELVOCs), low-volatility
574 organic compounds (LVOCs), semi-volatile organic compounds (SVOCs), and intermediate-volatility organic compounds
575 (IVOCs), delineated by their C^* values.
576
577
578

579
580
581
582
583
584
585
586
587
588
589
590
591
592
593
594
595



596
597 **Figure 6.** Time series plots of (a) MO-OOA concentration, (b) ozone (O_3) and solar radiation, (c) f_{44} and f_{43} (indicative of
598 oxidation state), and (d) total PM_1 concentration. The period characterized by elevated MO-OOA levels is highlighted in bright
599 yellow. Panels (e)–(f) present comparative distributions of these variables—MO-OOA, O_3 and solar radiation, f_{44} and f_{43} , and
600 PM_1 —between the high MO-OOA period (shaded in blue) and the entire measurement period (indicated by gray hatching).

601
602
603
604
605

606
607
608
609
610
611
612
613
614
615

616 **References**

617 Ghim, Y. S., Moon, K.-C., Lee, S., Kim, Y. P., 2005. Visibility trends in Korea during the past two decades. *J. Air Waste*
618 *Manag. Assoc.* 55, 73–82. <https://doi.org/10.1080/10473289.2005.10464599>

619 Zhao, H., Che, H., Zhang, X., Ma, Y., Wang, Y., Wang, H., Wang, Y., 2013. Characteristics of visibility and particulate matter
620 (PM) in an urban area of Northeast China. *Atmos. Pollut. Res.* 4, 427–434. <https://doi.org/10.5094/APR.2013.049>

621 Hamanaka, R. B., Mutlu, G. M., 2018. Particulate matter air pollution: Effects on the cardiovascular system. *Front. Endocrinol.*
622 9, 680. <https://doi.org/10.3389/fendo.2018.00680>

623 Manisalidis, I., Stavropoulou, E., Stavropoulos, A., Bezirtzoglou, E., 2020. Environmental and health impacts of air pollution:
624 a review. *Front. Public Health* 8, 14. <https://doi.org/10.3389/fpubh.2020.00014>

625 IPCC, 2021. Climate Change 2021: The Physical Science Basis. Contribution of Working Group I to the Sixth Assessment
626 Report of the Intergovernmental Panel on Climate Change, edited by Masson-Delmotte, V., Zhai, P., Pirani, A., Connors,
627 S.L., Péan, C., Berger, S., et al. Cambridge University Press, Cambridge, UK and New York, NY, USA, pp. 817–922.
628 <https://doi.org/10.1017/9781009157896.008>

629 Zhang, Q., Jimenez, J. L., Canagaratna, M. R., Allan, J. D., Coe, H., Ulbrich, I., Alfarra, M. R., Takami, A., Middlebrook, A.
630 M., Sun, Y. L., Dzepina, K., Dunlea, E., Docherty, K., DeCarlo, P., Salcedo, D., Onasch, T. B., Jayne, J. T., Miyoshi, T.,
631 Shimono, A., Hatakeyama, N., Takegawa, N., Kondo, Y., Schneider, J., Drewnick, F., Weimer, S., Demerjian, K. L.,
632 Williams, P. I., Bower, K. N., Bahreini, R., Cottrell, L., Griffin, R. J., Rautianen, J., Worsnop, D. R., 2007. Ubiquity and
633 dominance of oxygenated species in organic aerosols in anthropogenically-influenced Northern Hemisphere mid-latitudes.
634 *Geophys. Res. Lett.* 34, L13801. <https://doi.org/10.1029/2007GL029979>

635 Jimenez, J. L., Canagaratna, M. R., Donahue, N. M., Prevot, A. S. H., Zhang, Q., Kroll, J. H., ... Worsnop, D. R., 2009.
636 Evolution of organic aerosols in the atmosphere. *Science* 326, 1525–1529. <https://doi.org/10.1126/science.1180353>

Formatted: Font color: Auto

Formatted: Font color: Auto

Field Code Changed

Formatted: Font color: Auto

Field Code Changed

Formatted: Font color: Auto

Formatted: Font color: Auto

637 Hallquist, M., Wenger, J. C., Baltensperger, U., Rudich, Y., Simpson, D., Claeys, M., ... Seinfeld, J. H., 2009. The formation,
638 properties and impact of secondary organic aerosol: current and emerging issues. *Atmos. Chem. Phys.* 9, 5155–5236.
639 <https://doi.org/10.5194/acp-9-5155-2009>

640 Robinson, A. L., Donahue, N. M., Shrivastava, M. K., Weitkamp, E. A., Sage, A. M., Grieshop, A. P., Lane, T. E., Pierce, J.
641 R., Pandis, S. N., 2007. Rethinking organic aerosols: Semivolatile emissions and photochemical aging. *Science* 315, 1259–
642 1262. <https://doi.org/10.1126/science.1133061>

643 Donahue, N. M., Robinson, A. L., Stanier, C. O., Pandis, S. N., 2006. Coupled partitioning, dilution, and chemical aging of
644 semivolatile organics. *Environ. Sci. Technol.* 40, 2635–2643. <https://doi.org/10.1021/es052297c>

645 Ng, N. L., Canagaratna, M. R., Zhang, Q., Jimenez, J. L., Tian, J., Ulbrich, I. M., Kroll, J. H., Docherty, K. S., Chhabra, P. S.,
646 Bahreini, R., Murphy, S. M., Seinfeld, J. H., Hildebrandt, L., Donahue, N. M., DeCarlo, P. F., Lanz, V. A., Prévôt, A. S.
647 H., Dinar, E., Rudich, Y., Worsnop, D. R., 2010. Organic aerosol components observed in Northern Hemispheric datasets
648 from Aerosol Mass Spectrometry. *Atmos. Chem. Phys.* 10, 4625–4641. <https://doi.org/10.5194/acp-10-4625-2010>

649 Cappa, C. D., Jimenez, J. L., 2010. Quantitative estimates of the volatility of ambient organic aerosol. *Atmos. Chem. Phys.*
650 10, 5409–5424. <https://doi.org/10.5194/acp-10-5409-2010>

651 Sinha, A., George, I., Holder, A., Preston, W., Hays, M., Grieshop, A. P., 2023. Development of volatility distributions for
652 organic matter in biomass burning emissions. *Environ. Sci. Adv.* 3, 11–23. <https://doi.org/10.1039/D2EA00080F>

653 Glasius, M., Goldstein, A. H., 2016. Recent discoveries and future challenges in atmospheric organic chemistry. *Environ. Sci.
654 Technol.* 50, 2754–2764. <https://doi.org/10.1021/acs.est.5b05105>

655 Matsui, H., Koike, M., Takegawa, N., Kondo, Y., Griffin, R. J., Miyazaki, Y., Yokouchi, Y., Ohara, T., 2009. Secondary
656 organic aerosol formation in urban air: Temporal variations and possible contributions from unidentified hydrocarbons. *J.
657 Geophys. Res. Atmos.* 114, D02209. <https://doi.org/10.1029/2008JD010164>

658 Jiang, F., Liu, Q., Huang, X., Wang, T., Zhuang, B., Xie, M., 2012. Regional modelling of secondary organic aerosol over
659 China using WRF/Chem. *J. Aerosol Sci.* 53, 50–61. <https://doi.org/10.1016/j.jaerosci.2011.09.003>

660 Li, J., Zhang, M., Wu, F., Sun, Y., Tang, G., 2017. Assessment of the impacts of aromatic VOC emissions and yields of SOA
661 on SOA concentrations with the air quality model RAMS-CMAQ. *Atmos. Environ.* 158, 105–115.
662 <https://doi.org/10.1016/j.atmosenv.2017.03.035>

663 Zhao, B., Wang, S., Donahue, N. M., Jathar, S. H., Huang, X., Wu, W., ... & Hao, J. (2016). Quantifying the effect of organic
664 aerosol aging and intermediate-volatility emissions on regional-scale aerosol pollution in China. *Scientific Reports*, 6,
665 28815. <https://doi.org/10.1038/srep28815>

666 Kang, H. G., Kim, Y., Collier, S., Zhang, Q., Kim, H., 2022. Volatility of springtime ambient organic aerosol derived with
667 thermodenunder aerosol mass spectrometry in Seoul, Korea. *Environ. Pollut.* 310, 119203.
668 <https://doi.org/10.1016/j.envpol.2022.119203>

669 Huang, X.-F., He, L.-Y., Hu, M., Canagaratna, M. R., Sun, Y., Zhang, Q., Worsnop, D. R., 2010. Highly time-resolved
670 chemical characterization of atmospheric submicron particles during 2008 Beijing Olympic Games using an Aerodyne

Formatted: Font color: Auto

Formatted: Font color: Auto

Field Code Changed

Field Code Changed

Formatted: Font color: Auto

Formatted: Font color: Auto

Formatted: Font color: Auto

Formatted: Font color: Auto

Field Code Changed

671 High-Resolution Aerosol Mass Spectrometer. *Atmos. Chem. Phys.* 10, 8933–8945. <https://doi.org/10.5194/acp-10-8933-2010>

672

673 Mohr, C., DeCarlo, P. F., Heringa, M. F., Chirico, R., Slowik, J. G., Richter, R., Reche, C., Alastuey, A., Querol, X., Seco, R., Peñuelas, J., Jiménez, J. L., Crippa, M., Zimmermann, R., Baltensperger, U., Prévôt, A. S. H., 2012. Identification and quantification of organic aerosol from cooking and other sources in Barcelona using aerosol mass spectrometer data. *Atmos. Chem. Phys.* 12, 1649–1665. <https://doi.org/10.5194/acp-12-1649-2012>

674

675

676

677 Xu, L., Kollman, M. S., Song, C., Shilling, J. E., Ng, N. L., 2014. Effects of NO_x on the volatility of secondary organic aerosol from isoprene photooxidation. *Environ. Sci. Technol.* 48, 2253–2262. <https://doi.org/10.1021/es404842g>

678

679 Grieshop, A. P., Logue, J. M., Donahue, N. M., Robinson, A. L., 2009. Laboratory investigation of photochemical oxidation of organic aerosol from wood fires 1: Measurement and simulation of organic aerosol evolution. *Atmos. Chem. Phys.* 9, 1263–1277. <https://doi.org/10.5194/acp-9-1263-2009>

680

681

682 Kim, H., Zhang, Q., Bae, G.-N., Kim, J.Y., Lee, S.B., 2017. Sources and atmospheric processing of winter aerosols in Seoul, Korea: Insights from real-time measurements using a high-resolution aerosol mass spectrometer. *Atmos. Chem. Phys.* 17, 2009–2033. <https://doi.org/10.5194/acp-17-2009-2017>

683

684

685 DeCarlo, P. F., Kimmel, J. R., Trimborn, A., Northway, M. J., Jayne, A. E., Aiken, A. C., ... & Jimenez, J. L. (2006). Field-deployable, high-resolution, time-of-flight aerosol mass spectrometer. *Analytical Chemistry*, 78(24), 8281–8289. <https://doi.org/10.1021/ac061249>

686

687

688 Canagaratna, M. R., Jimenez, J. L., Kroll, J. H., Chen, Q., Kessler, S. H., Massoli, P., ... & Worsnop, D. R. (2015). Elemental ratio measurements of organic compounds using aerosol mass spectrometry: Improved sensitivity and intercomparability. *Atmospheric Chemistry and Physics*, 15(1), 253–272. <https://doi.org/10.5194/acp-15-253-2015>

689

690

691 Paatero, P., Tapper, U., 1994. Positive matrix factorization – A nonnegative factor model with optimal utilization of error estimates of data values. *Environmetrics* 5, 111–126. <https://doi.org/10.1002/env.3170050203>

692

693 Ulbrich, I. M., Canagaratna, M. R., Zhang, Q., Worsnop, D. R., Jimenez, J. L., 2009. Interpretation of organic components from Positive Matrix Factorization of aerosol mass spectrometric data. *Atmos. Chem. Phys.* 9, 2891–2918. <https://doi.org/10.5194/acp-9-2891-2009>

694

695

696 Zhang, Q., Jimenez, J. L., Canagaratna, M. R., Ulbrich, I. M., Ng, N. L., Worsnop, D. R., Sun, Y., 2011. Understanding atmospheric organic aerosols via factor analysis of aerosol mass spectrometry: A review. *Anal. Bioanal. Chem.* 401, 3045–3067. <https://doi.org/10.1007/s00216-011-5355-y>

697

698

699 Huffman, J. A., Docherty, K. S., Aiken, A. C., Cubison, M. J., Ulbrich, I. M., DeCarlo, P. F., Jimenez, J. L., 2009. Chemically-resolved aerosol volatility measurements from two megacity field studies. *Atmos. Chem. Phys.* 9, 7161–7182. <https://doi.org/10.5194/acp-9-7161-2009>

700

701

702 Saha, P. K., Khlystov, A., Grieshop, A. P., 2014. Determining aerosol volatility parameters using a “dual thermodenuder” system: Application to laboratory-generated organic aerosols. *Aerosol Sci. Technol.* 49, 620–632. <https://doi.org/10.1080/02786826.2015.1056769>

703

704

Formatted: Font color: Auto

Formatted: Font color: Auto

Field Code Changed

Field Code Changed

Formatted: Font color: Auto

Formatted: Font color: Auto

Formatted: Font color: Auto

Formatted: Font color: Auto

Field Code Changed

705 Zhou, S., Collier, S., Jaffe, D. A., Briggs, N. L., Hee, J., Sedlacek III, A. J., Kleinman, L., & Lewis, K., 2017. Regional
706 influence of wildfires on aerosol chemistry in the western US and insights into atmospheric aging of biomass burning
707 organic aerosol. *Atmospheric Chemistry and Physics*, 17, 2477–2493. <https://doi.org/10.5194/acp-17-2477-2017>

708 Riipinen, I., Pierce, J. R., Donahue, N. M., Pandis, S. N., 2010. Equilibration time scales of organic aerosol inside
709 thermodenuders: Kinetics versus equilibrium thermodynamics. *Atmos. Environ.* 44, 597–607.
710 <https://doi.org/10.1016/j.atmosenv.2009.11.022>

711 Karnezi, E., Riipinen, I., Pandis, S. N., 2014. Measuring the atmospheric organic aerosol volatility distribution: a theoretical
712 analysis. *Atmos. Meas. Tech.* 7, 2953–2965. <https://doi.org/10.5194/amt-7-2953-2014>

713 Chen, Y., Wang, Z., Wang, Y., Zheng, X., Fu, P., Kawamura, K., Zhang, Y., 2021. Characterization of nitrogen-containing
714 organic aerosol in Guangzhou, China: seasonal variation, formation mechanism and source apportionment. *Atmos. Chem.
715 Phys.* 21, 4329–4344. <https://doi.org/10.5194/acp-21-4329-2021>

716 Hayes, P. L., Ortega, A. M., Cubison, M. J., Froyd, K. D., Zhao, Y., Cliff, S. S., ... Jimenez, J. L., 2013. Organic aerosol
717 composition and sources in Pasadena, California, during the 2010 CalNex campaign. *J. Geophys. Res. Atmos.* 118, 9233–
718 9257. <https://doi.org/10.1002/2012JD017530>

719 Sun, Y., Jiang, Q., Wang, Z., Fu, P., Li, J., Yang, T., Yin, Y., 2011. Investigation of the sources and evolution processes of
720 severe haze pollution in Beijing in January 2013. *J. Geophys. Res. Atmos.* 119, 4380–4398.
721 <https://doi.org/10.1029/2014JD021641>

722 Baek, K. M., Park, E. H., Kang, H., Ji, M. J., Park, H. M., Heo, J & Kim, H., 2022. Seasonal characteristics of atmospheric
723 water-soluble organic nitrogen in PM2.5 in Seoul, Korea: Source and atmospheric processes of free amino acids and
724 aliphatic amines. *Science of the Total Environment*, 807, 150785. <https://doi.org/10.1016/j.scitotenv.2021.150785>

725 Rovelli, G., Miles, R. E. H., Reid, J. P., and Clegg, S. L.: Hygroscopic properties of aminium sulfate aerosols, *Atmos. Chem.
726 Phys.*, 17, 4369–4385, <https://doi.org/10.5194/acp-17-4369-2017>, 2017.

727 Ge, X., Wexler, A. S., Clegg, S. L., 2011. Atmospheric amines – Part I. A review. *Atmos. Environ.* 45, 524–546.
728 <https://doi.org/10.1016/j.atmosenv.2010.10.012>

729 He, J., Liu, H., Shan, P., Zhang, K., Qin, Y., & Liu, L. 2016. Supported-gas-membrane process for removal and recovery of
730 aliphatic amines from aqueous streams. *Chemical Engineering Science*, 144, 110–119.
731 <https://doi.org/10.1016/j.ces.2016.01.018>

732 You, Y., Renbaum-Wolff, L., Carreras-Sospedra, M., Dabdub, D., Bertram, A. K., Martin, S. T., et al., 2014. Images reveal
733 that amines promote the heterogeneous reaction of epoxides in model organic aerosols. *J. Phys. Chem. Lett.* 5, 3211–
734 3215. <https://doi.org/10.1021/jz501268k>

735 Yao, L., Wang, M. Y., Wang, X. K., Zhang, W. Q., Liu, Y., Li, L., et al., 2016. Atmospheric new particle formation from
736 sulfuric acid and amines in a Chinese megacity. *Sci. Bull.* 61, 939–945. <https://doi.org/10.1007/s11434-016-1083-0>

Field Code Changed
Formatted: Font color: Auto
Formatted: Font color: Auto

Field Code Changed
Formatted: Font color: Auto
Formatted: Font color: Auto

Formatted: Font color: Auto
Formatted: Font color: Auto
Field Code Changed
Field Code Changed
Formatted: Font color: Auto
Formatted: Font color: Auto

Field Code Changed
Formatted: Font color: Auto
Formatted: Font color: Auto
Field Code Changed
Formatted: Font color: Auto
Formatted: Font color: Auto
Field Code Changed
Formatted: Font color: Auto
Formatted: Font color: Auto

737 Kim, H., Zhang, Q., Sun, Y., Bae, G. N., Lee, B. E., Park, K., ... & Kim, Y. J. 2020. Measurement report: Characterization of
738 severe spring haze episodes and influences of long-range transport in the Seoul metropolitan area in March 2019.
739 *Atmospheric Chemistry and Physics*, 20(18), 11527–11545. <https://doi.org/10.5194/acp-20-11527-2020>

740 Jeon, J., Chen, Y., Kim, H., 2023. Influence of meteorology on emission sources and physicochemical properties of particulate
741 matter in Seoul, Korea during heating period. *Atmos. Environ.* 301, 119733.
742 <https://doi.org/10.1016/j.atmosenv.2023.119733>

743 Zhang, Q., Alfarra, M. R., Worsnop, D. R., Allan, J. D., Coe, H., Canagaratna, M. R., ... & Jimenez, J. L. 2005. Deconvolution
744 and quantification of hydrocarbon-like and oxygenated organic aerosols based on aerosol mass spectrometry.
745 *Environmental Science & Technology*, 39(13), 4938–4952. <https://doi.org/10.1021/es0485681>

746 Simoneit, B. R. T. 2002. Biomass burning – a review of organic tracers for smoke from incomplete combustion. *Applied
747 Geochemistry*, 17(3), 129–162. [https://doi.org/10.1016/S0883-2927\(01\)00061-0](https://doi.org/10.1016/S0883-2927(01)00061-0)

748 Cubison, M. J., Ortega, A. M., Hayes, P. L., Farmer, D. K., Day, D., Lechner, M. J., ... & Jimenez, J. L. 2011. Effects of aging
749 on organic aerosol from open biomass burning smoke in aircraft and laboratory studies. *Atmospheric Chemistry and
750 Physics*, 11(23), 12049–12064. <https://doi.org/10.5194/acp-11-12049-2011>

751 Xu, L., Williams, L. R., Young, D. E., Allan, J. D., Coe, H., Massoli, P., Fortner, E., Chhabra, P., Herndon, S., Brooks, W. A.,
752 Jayne, J. T., Worsnop, D. R., Aiken, A. C., Liu, S., Gorkowski, K., Dubey, M. K., Fleming, Z. L., Visser, S., Prévôt, A.
753 S. H., Ng, N. L., 2016. Wintertime aerosol chemical composition, volatility, and spatial variability in the Greater London
754 Area. *Atmos. Chem. Phys.* 16, 1139–1160. <https://doi.org/10.5194/acp-16-1139-2016>

755 Feng, T., Wang, Y., Hu, W., Zhu, M., Song, W., Chen, W., ... Wang, X., 2023. Impact of aging on the sources, volatility, and
756 viscosity of organic aerosols in Chinese outflows. *Atmos. Chem. Phys.* 23, 611–636. <https://doi.org/10.5194/acp-23-611-2023>

757

758 Scott, W. D., & Cattell, F. C. R. 1979. Vapor pressure of ammonium sulfates. *Atmospheric Environment* (1967), 13(6), 987–
759 1000. [https://doi.org/10.1016/0004-6981\(79\)90174-4](https://doi.org/10.1016/0004-6981(79)90174-4)

760 Donahue, N. M., Robinson, A. L., Pandis, S. N., 2009. Atmospheric organic particulate matter: From smoke to secondary
761 organic aerosol. *Atmos. Environ.* 43, 94–106. <https://doi.org/10.1016/j.atmosenv.2008.09.055>

762 Ehn, M., Thornton, J. A., Kleist, E., Sipilä, M., Junninen, H., Pullinen, I., ... & Kulmala, M. 2014. A large source of low-
763 volatility secondary organic aerosol. *Nature*, 506(7489), 476–479. <https://doi.org/10.1038/nature13032>

764 Kroll, J. H., Smith, J. D., Che, D. L., Kessler, S. H., Worsnop, D. R., Wilson, K. R., 2009. Measurement of fragmentation and
765 functionalization pathways in the heterogeneous oxidation of oxidation organic aerosol. *Environ. Sci. Technol.* 43, 7826–
766 7833. <https://doi.org/10.1021/es901683r>

767 Xu, L., Williams, L.R., Young, D.E., Allan, J.D., Coe, H., Massoli, P., Fortner, E., Chhabra, P., Herndon, S., Brooks, W.A.,
768 et al., 2016. Wintertime aerosol chemical composition, volatility, and spatial variability in the greater London area. *Atmos.
769 Chem. Phys.* 16, 1139–1160. <https://doi.org/10.5194/acp-16-1139-2016>

Field Code Changed
Formatted: Font color: Auto
Formatted: Font color: Auto
Field Code Changed
Formatted: Font color: Auto
Formatted: Font color: Auto
Formatted: Font color: Auto
Formatted: Font color: Auto
Field Code Changed

Field Code Changed
Formatted: Font color: Auto
Formatted: Font color: Auto

Field Code Changed
Formatted: Font color: Auto
Formatted: Font color: Auto
Field Code Changed
Formatted: Font color: Auto
Formatted: Font color: Auto
Formatted: Font color: Auto

770 Cao, L.-M., Huang, X.-F., Li, Y.-Y., Hu, M., He, L.-Y., 2018. Volatility measurement of atmospheric submicron aerosols in
771 an urban atmosphere in southern China. *Atmos. Chem. Phys.* 18, 1729–1743. <https://doi.org/10.5194/acp-18-1729-2018>

772 Xu, W., Xie, C., Karnezi, E., Zhang, Q., Wang, J., Pandis, S.N., Ge, X., Zhang, J., An, J., Wang, Q., et al., 2019. Summertime
773 aerosol volatility measurements in Beijing, China. *Atmos. Chem. Phys.* 19, 10205–10216. <https://doi.org/10.5194/acp-19-10205-2019>

775

776 [Allan, J. D., Alfarra, M. R., Bower, K. N., Williams, P. I., Gallagher, M. W., Jimenez, J. L., McDonald, A. G., Nemitz, E., Canagaratna, M. R., and Coe, H.: Quantitative sampling using an Aerodyne aerosol mass spectrometer—2. Measurements of fine particulate chemical composition in two U.K. cities, *J. Geophys. Res.-Atmos.*, 108, 4091, 2003, <https://doi.org/10.1029/2002JD002359>.](#)

777

778 [Berndt, T., Richters, S., Jokinen, T., et al.: Hydroxyl radical-induced formation of highly oxidized organic compounds, *Nat. Commun.*, 7, 13677, 2016, <https://doi.org/10.1038/ncomms13677>.](#)

779

780 [Bianchi, F., Kurtén, T., Riva, M., et al.: Highly oxygenated organic molecules \(HOM\) from gas-phase autoxidation involving peroxy radicals: A key contributor to atmospheric aerosol, *Chem. Rev.*, 119, 3472–3509, 2019, <https://doi.org/10.1021/acs.chemrev.8b00395>.](#)

781

782 [Brown, S. S. and Stutz, J.: Nighttime radical observations and chemistry, *Chem. Soc. Rev.*, 41, 6405–6447, 2012, <https://doi.org/10.1039/C2CS35181A>.](#)

783

784 [Canagaratna, M. R., Jayne, J. T., Jimenez, J. L., et al.: Chemical and microphysical characterization of ambient aerosols with the Aerodyne aerosol mass spectrometer, *Mass Spectrom. Rev.*, 26, 185–222, 2007, <https://doi.org/10.1002/mas.20115>.](#)

785

786 [Chhabra, P. S., Ng, N. L., Canagaratna, M. R., et al.: Elemental composition and oxidation of chamber organic aerosol, *Atmos. Chem. Phys.*, 11, 8827–8841, 2011, <https://doi.org/10.5194/acp-11-8827-2011>.](#)

787

788 [D'Ambro, E. L., Schobesberger, S., Gaston, C. J., et al.: Molecular composition and volatility of isoprene photochemical oxidation secondary organic aerosol under low- and high-NO_x conditions, *Atmos. Chem. Phys.*, 17, 159–174, 2017, <https://doi.org/10.5194/acp-17-159-2017>.](#)

789

790 [Donahue, N. M., Epstein, S. A., Pandis, S. N., and Robinson, A. L.: A two-dimensional volatility basis set – Part 1: Organic-aerosol mixing thermodynamics, *Atmos. Chem. Phys.*, 11, 3303–3318, 2011, <https://doi.org/10.5194/acp-11-3303-2011>.](#)

791

792 [Faulhaber, A. E., Thomas, B. M., Jimenez, J. L., et al.: Characterization of a thermodenuder–particle beam mass spectrometer system for the study of organic aerosol volatility and composition, *Atmos. Meas. Tech.*, 2, 15–31, 2009, <https://doi.org/10.5194/amt-2-15-2009>.](#)

793

794 [Ge, X., Wexler, A. S., and Clegg, S. L.: Atmospheric amines – Part III: Photochemistry and toxicity, *Atmos. Environ.*, 45, 561–591, 2011, <https://doi.org/10.1016/j.atmosenv.2010.11.050>.](#)

795

796 [Gil, J., Lee, Y., and Kim, Y. P.: Characteristics of HONO and its impact on O₃ formation in the Seoul Metropolitan Area during KORUS-AQ, *Atmos. Environ.*, 246, 118032, 2021, <https://doi.org/10.1016/j.atmosenv.2020.118032>.](#)

797

798

799

800

801

Formatted: Font color: Auto

Formatted: Font color: Auto

Formatted: Font color: Auto

Formatted: Font color: Auto

803 Han, K.-M., Kim, D.-G., Kim, J., et al.: Crop residue burning emissions and impact on particulate matter over South Korea, *Atmosphere*, 13, 559, 2022, <https://doi.org/10.3390/atmos13040559>.

804

805 Hanson, D. R., McMurry, P. H., Jiang, J., et al.: Ambient pressure proton transfer mass spectrometry: detection of amines and *Environ. Sci. Technol.*, 45, 8881–8888, 2011, <https://doi.org/10.1021/es2018817>.

806

807 Hennigan, C. J., Sullivan, A. P., Collett, J. L., Jr., and Robinson, A. L.: Levoglucosan stability in biomass burning particles *exposed to hydroxyl radicals*, *Geophys. Res. Lett.*, 37, L09806, 2010, <https://doi.org/10.1029/2010GL043088>.

808

809 Huffman, J. A., Ziemann, P. J., Jayne, J. T., et al.: Development and characterization of a fast-stepping thermodenuder for *chemically resolved aerosol volatility measurements*, *Aerosol Sci. Technol.*, 42, 395–407, 2008, <https://doi.org/10.1080/02786820802104981>.

810

811

812 Kim, K., Park, R., Lee, Y., et al.: An investigation into atmospheric nitrous acid (HONO) and its sources in East Asia, *Atmos. Chem. Phys.*, 24, 12575–12593, 2024, <https://doi.org/10.5194/acp-24-12575-2024>.

813

814 Kroll, J. H. and Seinfeld, J. H.: Chemistry of secondary organic aerosol: Formation and evolution of low-volatility organics in *the atmosphere*, *Atmos. Environ.*, 42, 3593–3624, 2008, <https://doi.org/10.1016/j.atmosenv.2008.01.003>.

815

816 Kroll, J., Donahue, N., Jimenez, J., et al.: Carbon oxidation state as a metric for describing the chemistry of atmospheric *organic aerosol*, *Nat. Chem.*, 3, 133–139, 2011, <https://doi.org/10.1038/nchem.948>.

817

818 Kwon, S., Won, S. R., Lim, H. B., et al.: Relationship between PM1.0 and PM2.5 in urban and background areas of the *Republic of Korea*, *Atmos. Pollut. Res.*, 14, 101858, 2023, <https://doi.org/10.1016/j.apr.2023.101858>.

819

820 Lamb, K. D., Kim, B.-G., and Kim, S.-W.: Estimating source-region influences on black carbon in South Korea using the *BC/CO ratio*, *J. Geophys. Res.-Atmos.*, 123, 11, 2018, <https://doi.org/10.1029/2018JD029257>.

821

822 Lambe, A. T., Onasch, T. B., Massoli, P., et al.: Transitions from Functionalization to Fragmentation Reactions of Laboratory *Secondary Organic Aerosol (SOA)* Generated from the OH Oxidation of Alkane Precursors, *Environ. Sci. Technol.*, 46, 5430–5437, 2012, <https://doi.org/10.1021/es300274t>.

823

824

825 López-Hilfiker, F. D., Mohr, C., Ehn, M., et al.: A novel method for online analysis of gas and particle composition: description *and evaluation of a Filter Inlet for Gases and AERosols (FIGAERO)*, *Atmos. Meas. Tech.*, 7, 983–1001, 2014, <https://doi.org/10.5194/amt-7-983-2014>.

826

827

828 López-Hilfiker, F. D., Mohr, C., Ehn, M., et al.: Molecular composition and volatility of organic aerosol in the Southeastern *U.S.* using FIGAERO-CIMS with comparison to AMS, *Environ. Sci. Technol.*, 50, 2200–2209, 2016, <https://doi.org/10.1021/acs.est.5b04769>.

829

830

831 Mao, J., Wang, L., Lu, C., et al.: High-resolution modeling of gaseous methylamines over a polluted region in China: source-*dependent emissions and implications of spatial variations*, *Atmos. Chem. Phys.*, 18, 7933–7950, 2018, <https://doi.org/10.5194/acp-18-7933-2018>.

832

833

834 Matsui, H., Koike, M., Kondo, Y., et al.: An estimation of the organic aerosol component in PM2.5 using AMS and CMB *models*, *J. Geophys. Res.-Atmos.*, 114, D21203, 2009, <https://doi.org/10.1029/2009JD012170>.

835

836 Nault, B. A., Campuzano-Jost, P., Day, D. A., et al.: Secondary organic aerosol production from local emissions dominates
837 over Seoul during KORUS-AQ, *Atmos. Chem. Phys.*, 18, 17769–17800, 2018, <https://doi.org/10.5194/acp-18-17769-2018>.

838 Nielsen, C. J., Herrmann, H., and Weller, C.: Atmospheric chemistry and environmental impact of the use of amines in carbon
839 capture and storage (CCS), *Chem. Soc. Rev.*, 41, 6684–6704, 2012, <https://doi.org/10.1039/C2CS35059A>.

840 Slater, E. J., Gkatzoflias, D., Wang, Y., et al.: Elevated levels of OH observed in haze events during wintertime Beijing, *Atmos.*
841 *Chem. Phys.*, 20, 14847–14871, 2020, <https://doi.org/10.5194/acp-20-14847-2020>.

842 Sun, Y., Zhang, Q., Schwab, J. J., et al.: Characterization of the sources and properties of organic aerosol from AMS
843 measurements during a winter campaign in Beijing, China, *Atmos. Chem. Phys.*, 10, 8951–8971, 2010,
844 <https://doi.org/10.5194/acp-10-8951-2010>.

845 Tiszenkel, L., Flynn, J. H., and Lee, S.-H.: Measurement report: Urban ammonia and amines in Houston, Texas, *Atmos. Chem.*
846 *Phys.*, 24, 11351–11363, 2024, <https://doi.org/10.5194/acp-24-11351-2024>.

847 Yoo, H., Lee, H., and Kim, Y. P.: Insights from single-particle analysis: submicron aerosol composition in Seoul during
848 KORUS-AQ, *Atmos. Chem. Phys.*, 24, 853–872, 2024, <https://doi.org/10.5194/acp-24-853-2024>.

849 Ziemann, P. J. and Atkinson, R.: Kinetics, products, and mechanisms of secondary organic aerosol formation from gas-phase
850 reactions of organic compounds, *Chem. Soc. Rev.*, 41, 6582–6605, 2012, <https://doi.org/10.1039/C2CS35122F>.

851 Paciga, A., Young, D. E., Ward, M. W., et al.: Volatility of organic aerosol and its components in the megacity of Paris, *Atmos.*
852 *Chem. Phys.*, 16, 2013–2031, 2016, <https://doi.org/10.5194/acp-16-2013-2016>.

853 Ge, X., Wexler, A. S., and Clegg, S. L.: Atmospheric amines – Part II. Thermodynamic properties and gas-particle partitioning,
854 *Atmos. Chem. Phys.*, 11, 55–69, 2011, <https://doi.org/10.5194/acp-11-55-2011>.

855 Xu, W., Sun, Y., Wang, Q., et al.: Seasonal characterization of organic nitrogen in atmospheric aerosols using high-resolution
856 aerosol mass spectrometry in Beijing, China, *ACS Earth Space Chem.*, 1, 649–658, 2017,
857 <https://doi.org/10.1021/acsearthspacechem.7b00106>.

858 Sun, Y. L., Zhang, Q., Schwab, J. J., et al.: Characterization of the sources and processes of organic and inorganic aerosols in
859 New York City with a high-resolution time-of-flight aerosol mass spectrometer, *Atmos. Chem. Phys.*, 11, 1581–1602,
860 2011, <https://doi.org/10.5194/acp-11-1581-2011>.

861 Saarikoski, S., Carbone, S., Decesari, S., et al.: Chemical characterization of springtime submicrometer aerosol in Po Valley,
862 Italy, *Atmos. Chem. Phys.*, 12, 8401–8421, 2012, <https://doi.org/10.5194/acp-12-8401-2012>.

863 Silva, P. J., Erupe, M. E., Price, D., et al.: Trimethylamine as precursor to secondary organic aerosol formation via nitrate
864 radical reaction in the atmosphere, *Environ. Sci. Technol.*, 42, 4689–4696, 2008, <https://doi.org/10.1021/es703016v>

Formatted: Font color: Auto

Formatted: Font color: Auto